Supplementary Information

Understanding the oxygen reduction/evolution reactions (ORR/OER) on bimetallic Pt-Ir electrocatalysts using in-situ Raman spectroscopy and DFT

Sonja Blaseio[a], Thies Reetz[b], Halil İ. Sözen[b,c], Carsten Dosche[b], Christian Schneemann[a], Gustav Sievers[d], Martin Rohloff[d], Uta Schlickum[e], Thorsten Klüner[b], Mehtap Oezaslan[a*]

a Technical Electrocatalysis Laboratory, Institute of Physical Chemistry, Universität Hamburg, Grindelallee 117, 20146 Hamburg.

b Institute of Chemistry, University of Oldenburg, Carl-von-Ossietzky-Str. 9-11, 26129 Oldenburg, Germany.

c Mercedes-Benz Turk A.S., Orhan Gazi Mahallesi, Mercedes Bulvari No. 17/1, Esenyurt, Istanbul 34519, Turkey.

d elementarhy GmbH, Gustav-Adolf-Straße 78, 22043 Hamburg, Germany.

e Laboratory for Emerging Nanometrology, Institute of Applied Physics, Technische Universität Braunschweig, 38106 Braunschweig, Germany.

*Corresponding author: Prof. Mehtap Oezaslan (mehtap.oezaslan@uni-hamburg.de)

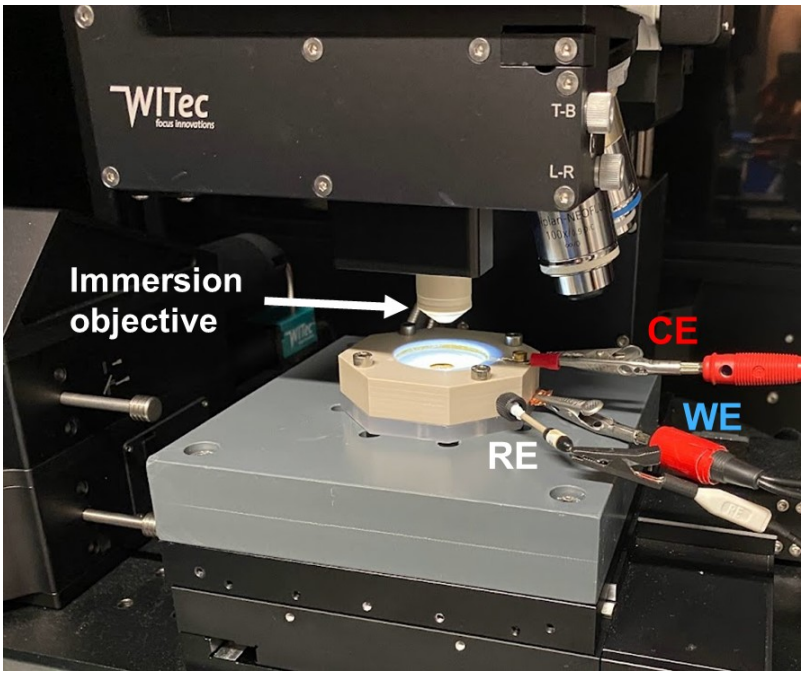

Fig. S1. Image of the in-situ custom-made three-electrode spectro-electrochemical Raman cell. Electrochemical measurements were conducted in 0.1 M $HClO_4$. Pt-Ir thin films sputtered on a GDL substrate were used as a working electrode (WE, blue). A gold mesh and a mercury-mercury sulfate (MMS) electrode were employed as counter (CE, red) and reference (RE, white) electrodes, respectively. The chronoamperometric protocol started from 0.3 V_{RHE} to 1.6 V_{RHE} with potential step of 100 mV. All reported potentials were corrected for the iR-drop.

Table S1. Experimental acquisition parameters for survey and high-resolution XPS measurements.

spectrum	energy range / eV	step size / eV	pass energy / eV	dwell time / ms	no. of scans
Survey	- 10 – 1350	1	100	10	5
Pt & Ir4f	55 – 85	0.02	10	50	20
O 1s	525 – 540	0.02	10	50	10
C 1s	279 – 298	0.02	10	50	5

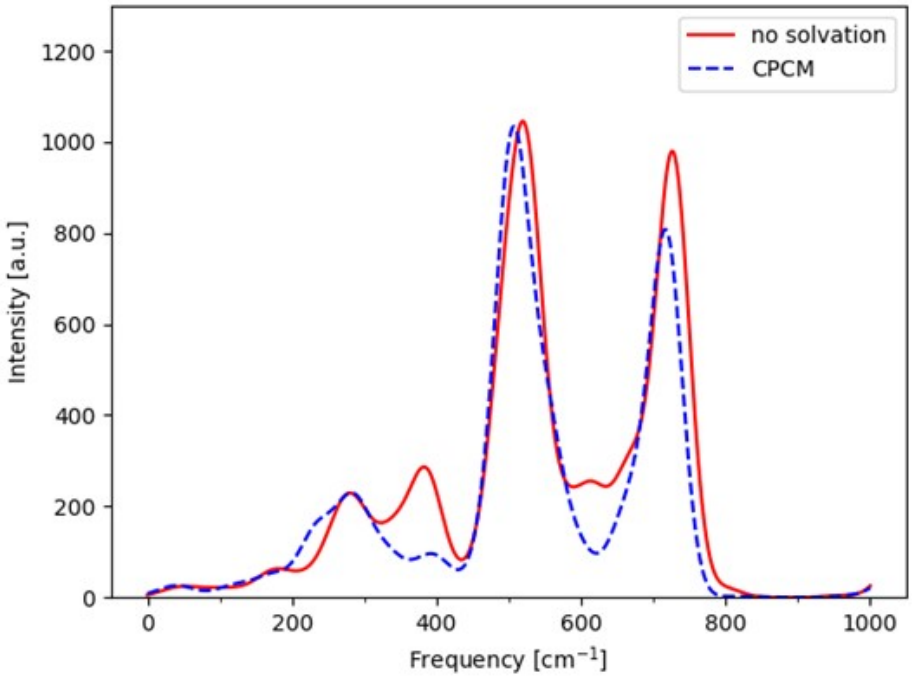

Fig. S2. Comparison of the predicted Raman spectra of the iridium oxo-hydroxy tetramer complex with (blue dashed line) and without (red solid line) implicit water solvation using the Conductor-like Polarizable Continuum Model (CPCM).

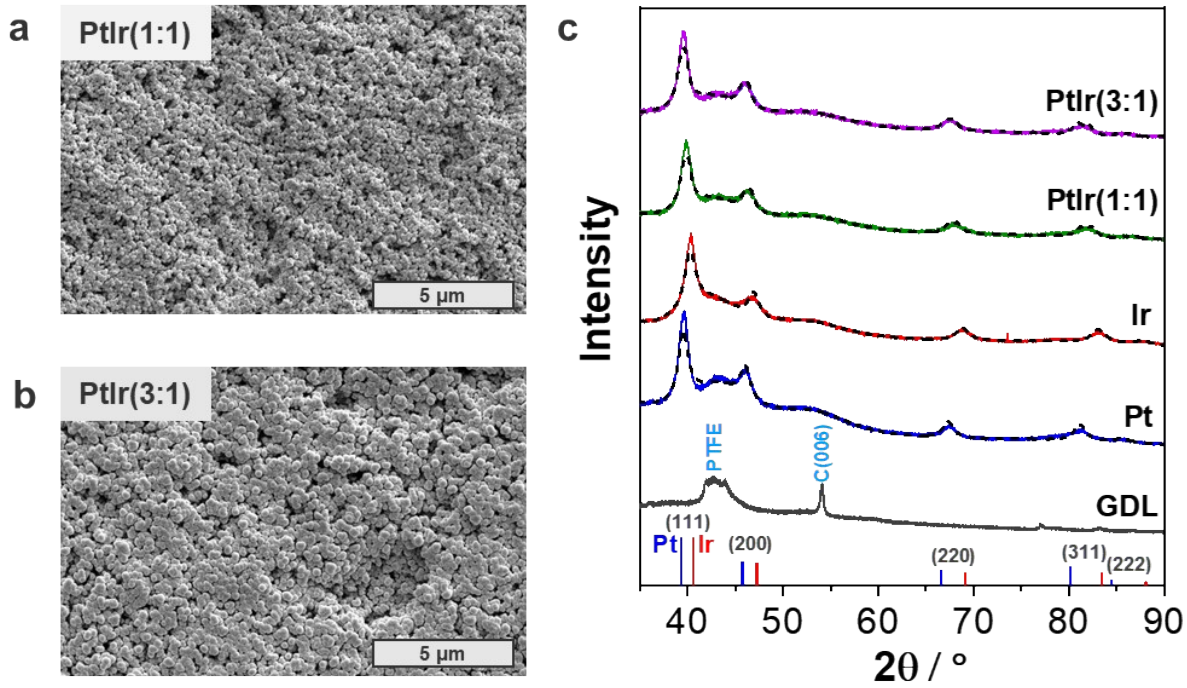

Fig. S3. (**a** and **b**) Top-view low magnification SEM micrographs of the Pt-Ir thin films with atomic Pt:Ir ratios of 1:1 and 3:1. (**c**) XRD profiles of the sputtered PtIr(1:1) (green), PtIr(3:1) (purple), Ir (red) and Pt (blue) thin films with the best fits (black dashed lines) obtained from the quantitative Rietveld refinement analysis. Note, that the peaks at 2θ values of around 42 – 44° and ~54° are ascribed to the amorphous PTFE and C(006) graphite of the GDL substrate, respectively. The pattern references of the face-centered cubic (fcc) Pt (#9008480, blue) and Ir (#9008470, red) were taken from the crystal open database (COD).[1–3]

Table S2. Thin film composition obtained by μ-XRF technique with three ~20 μm spot measurements. The characteristic L_α lines of Pt and Ir were used for quantitative.

sample	Pt content / at. %	Ir content / at. %
PtIr(1:1)	47 ± 2	53 ± 2
PtIr(3:1)	75 ± 1	25 ± 1
Pt	100	–
Ir	–	100

Table S3. Space group, lattice parameter, crystallite size, phase quantity and composition via Vegard's law determined by quantitative Rietveld refinement analysis of the XRD profiles for the Pt-Ir thin films displayed in **Fig. S2**. The weighted profile R-factor (R_{wp}) represents the discrepancy index between the calculated and measured data.

sample	space group	lattice parameter / Å	crystallite size / nm	quantity / wt.%	composition via Vegard's law	R_{wp}
PtIr(1:1)	$Fm\bar{3}m$	3.919 ± 0.001	6.1 ± 0.2	51 ± 1	$Pt_{95}Ir_{05}$	4.80
	$Fm\bar{3}m$	3.872 ± 0.001	7.2 ± 0.2	49 ± 1	$Pt_{40}Ir_{60}$	
PtIr(3:1)	$Fm\bar{3}m$	3.923 ± 0.001	6.0 ± 0.1	59 ± 1	$Pt_{100}Ir_{0}$	5.16
	$Fm\bar{3}m$	3.879 ± 0.001	8.2 ± 0.3	41 ± 1	$Pt_{52}Ir_{48}$	
Pt	$Fm\bar{3}m$	3.923 ± 0.001	5.1 ± 0.1	-	Pt_{100}	5.22
Ir	$Fm\bar{3}m$	3.841 ± 0.001	4.5 ± 0.1	-	Ir_{100}	4.70

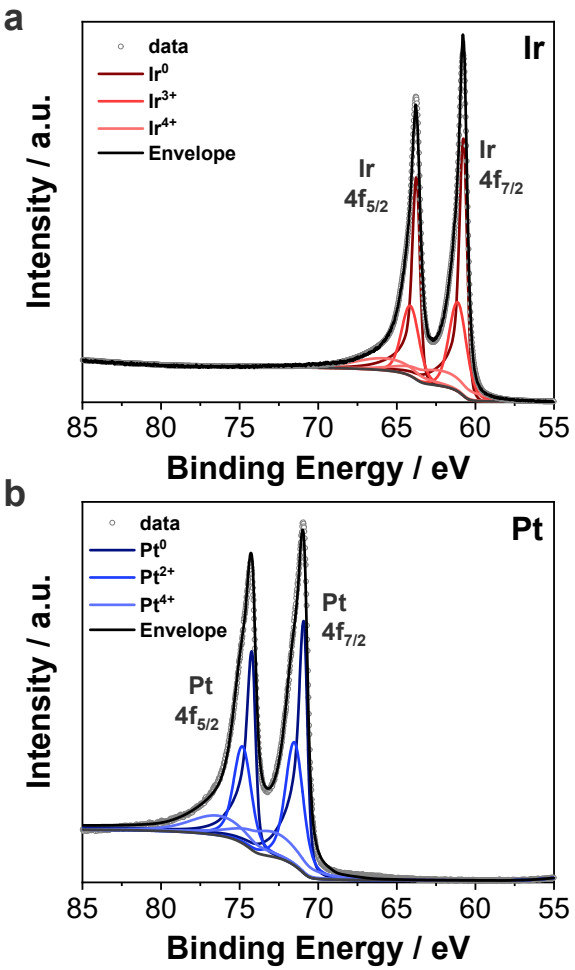

Fig. S4. Ex-situ high-resolution Ir and Pt 4f XPS spectra of the monometallic (**a**) Ir and (**b**) Pt thin films. Light grey circles represent the measured data, the envelope is shown in black. The Ir^0, Ir^{3+} and Ir^{4+} species are displayed in red, while the Pt^0, Pt^{2+} and Pt^{4+} species are plotted in blue.

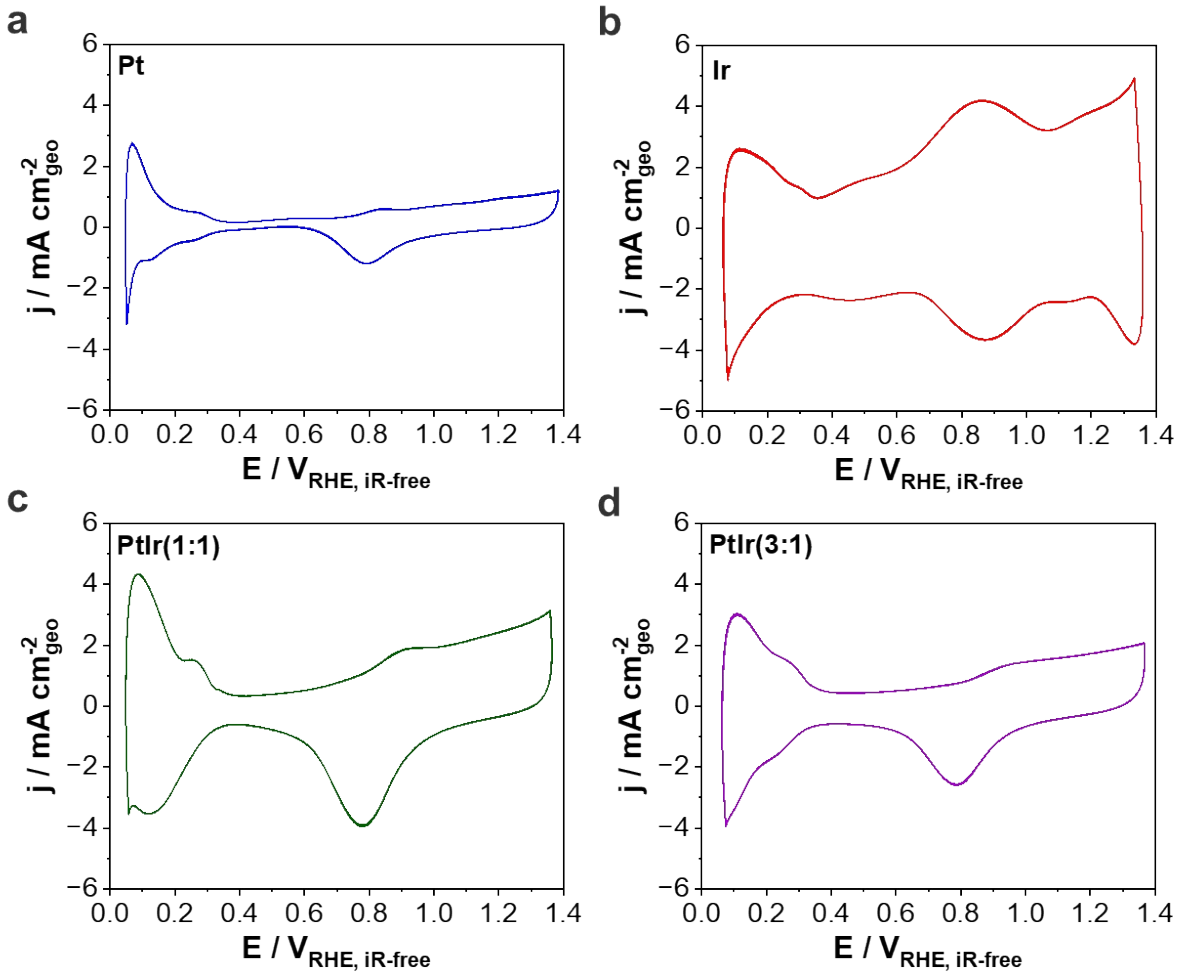

Fig. S5. Cyclic voltammetry (CV) profiles of the (**a**) Pt, (**b**) Ir, (**c**) PtIr(1:1) and (**d**) PtIr(3:1) thin films (total metal loading of 0.4 mg_{metal} cm^{-2}_{geo}) recorded at 50 mV s^{-1} using an impinging jet flow cell in static Ar-saturated 0.1 M $HClO_4$ solution electrolyte. The H_{UPD} region between 0.06 and 0.4 $V_{RHE,iR\text{-}free}$ is observed for all thin films.

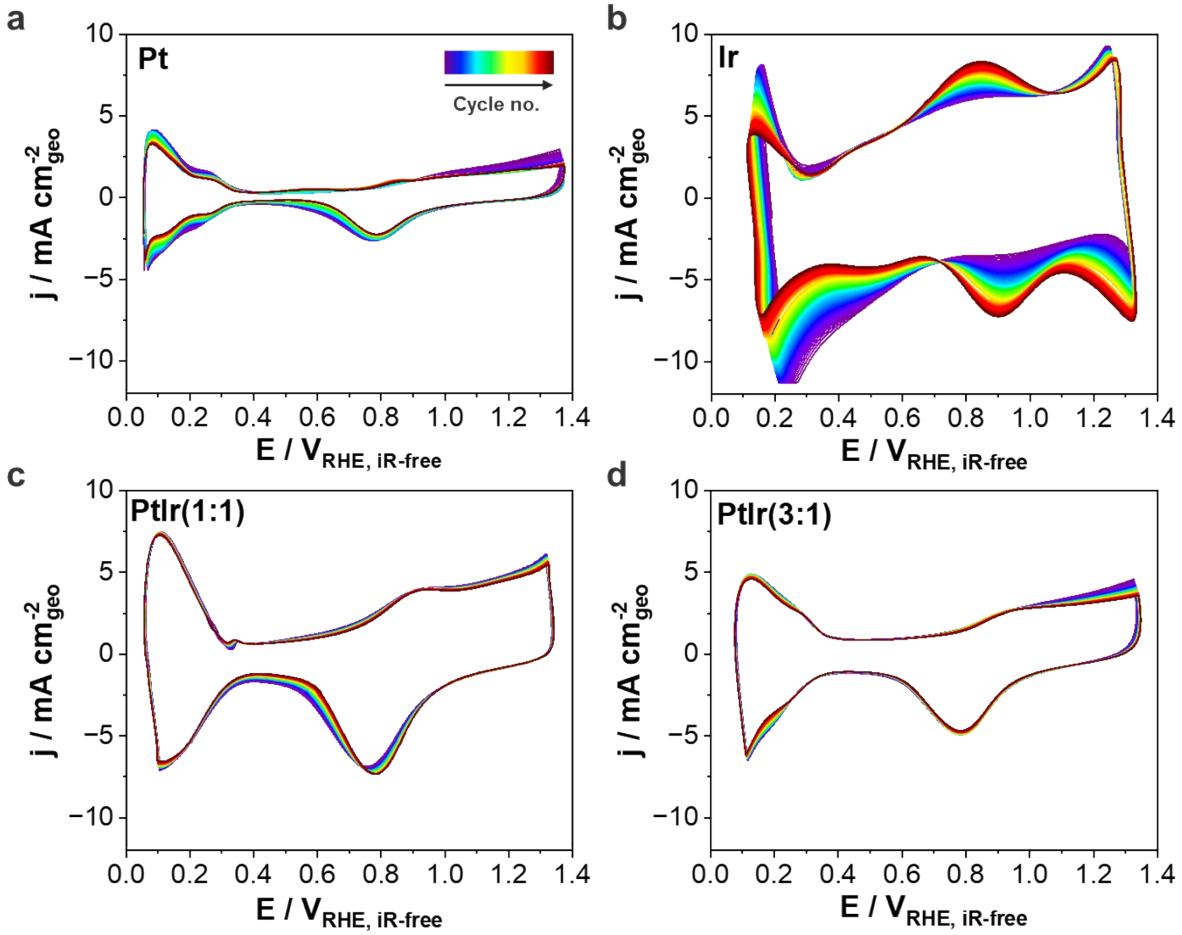

Fig. S6. Pre-conditioning protocol with 100 cyclic voltammetry (CV) profiles at 100 mV s^{-1} using an impinging jet flow cell in static Ar-saturated 0.1 M $HClO_4$ electrolyte. Evolution of the CV profiles of (**a**) Pt, (**b**) Ir, (**c**) PtIr(1:1) and (**d**) PtIr(3:1) thin films.

Table S4. Underpotential deposition of hydrogen (H_{UPD}) as well as ORR and OER specific activities (SA) of the Pt, PtIr(1:1), PtIr(3:1) and Ir thin films with a total metal loading of 0.4 mg_{metal} cm_{geo}^{-2}. The H_{UPD} was obtained from cyclic voltammetry measurements shown in **Fig. S4**. The roughness factor (RF) was obtained by dividing the H_{UPD} by the geometric surface area (0.196 cm^2). SA values towards ORR were determined at 0.90 $V_{RHE,\ iR\text{-}free}$ and towards OER at 1.50 $V_{RHE,\ iR\text{-}free}$.

sample	**H_{UPD} / cm^2**	**roughness factor (RF)**	**SA_{ORR} / µA cm_{HUP}^{-2} at 0.90 $V_{RHE,\ iR\text{-}free}$**	**SA_{OER} / µA cm_{HUP}^{-2} at 1.50 $V_{RHE,\ iR\text{-}free}$**
Pt	3.8 ± 0.2	19	54	5
PtIr(3:1)	7.6 ± 0.4	39	88	9
PtIr(1:1)	11.0 ± 0.2	56	57	34
Ir	5.0 ± 0.6	26	3	286

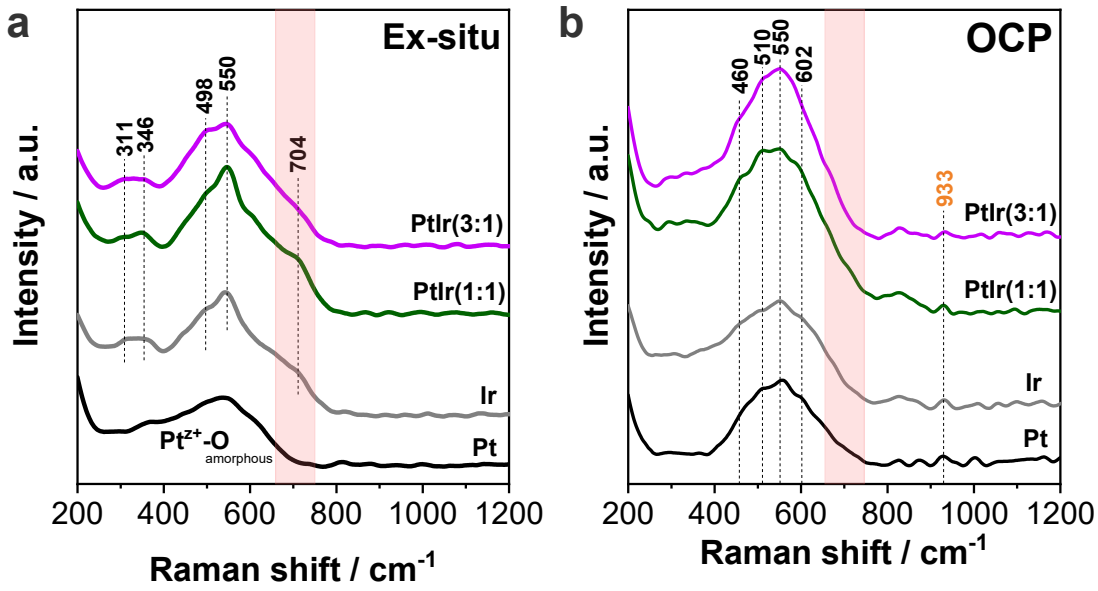

Fig. S7. Raman spectra of the PtIr(1:1) (green), PtIr(3:1) (pink), Pt (black) and Ir (grey) thin films obtained from (**a**) ex-situ and (**b**) in-situ at open circuit potential (OCP) in 0.1 M $HClO_4$. The peak labelled at 933 cm^{-1} is assigned to adsorbed $^{ClO^-_4}$ anion (**Fig. S8**). The colored red region shows the disappearance of the Raman band at 704 cm^{-1} with exposure to the electrolyte. Peak assignments are summarized in **Table S5**.

Table S5. Raman peaks and corresponding modes of vibration for both Pt-Ir, Pt and Ir thin-films obtained from the ex-situ and in-situ (at OCP) measurements, as shown in **Fig. S6**.

Raman shift / cm^{-1}	Mode of vibration	Ref.
311	Ir-O bend	4
346	Ir-O bend	4
460	ClO_4^- adsorbed on Ir surface	5,6
498	Ir^{4+}-O stretch	4
550	IrO_2 (E_g)	4,7,8
602	Ir^{3+}-OH-Ir^{4+} stretch	4
704	IrO_2 (B_{2g})	4,7,8
933	ClO_4^-, ads.	9–12

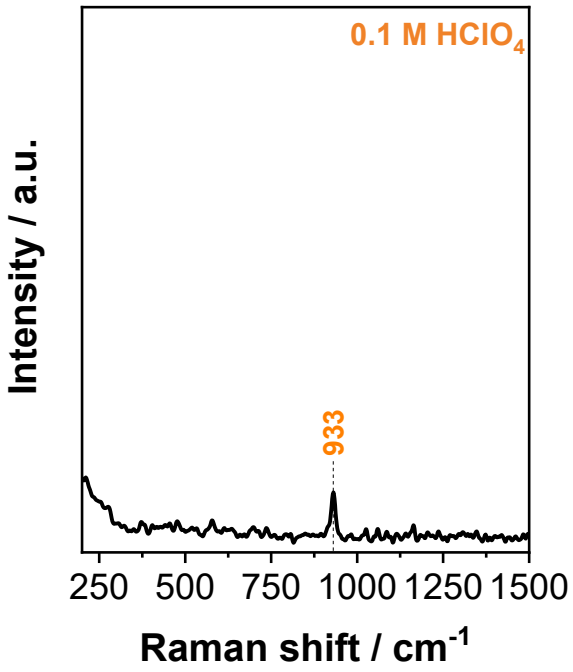

Fig. S8. Raman spectrum collected of 0.1 M $HClO_4$ electrolyte solution. The peak at 933 cm^{-1} is assigned to adsorbed ClO_4^-, which is in excellent agreement with the literature.[5,9,10,12]

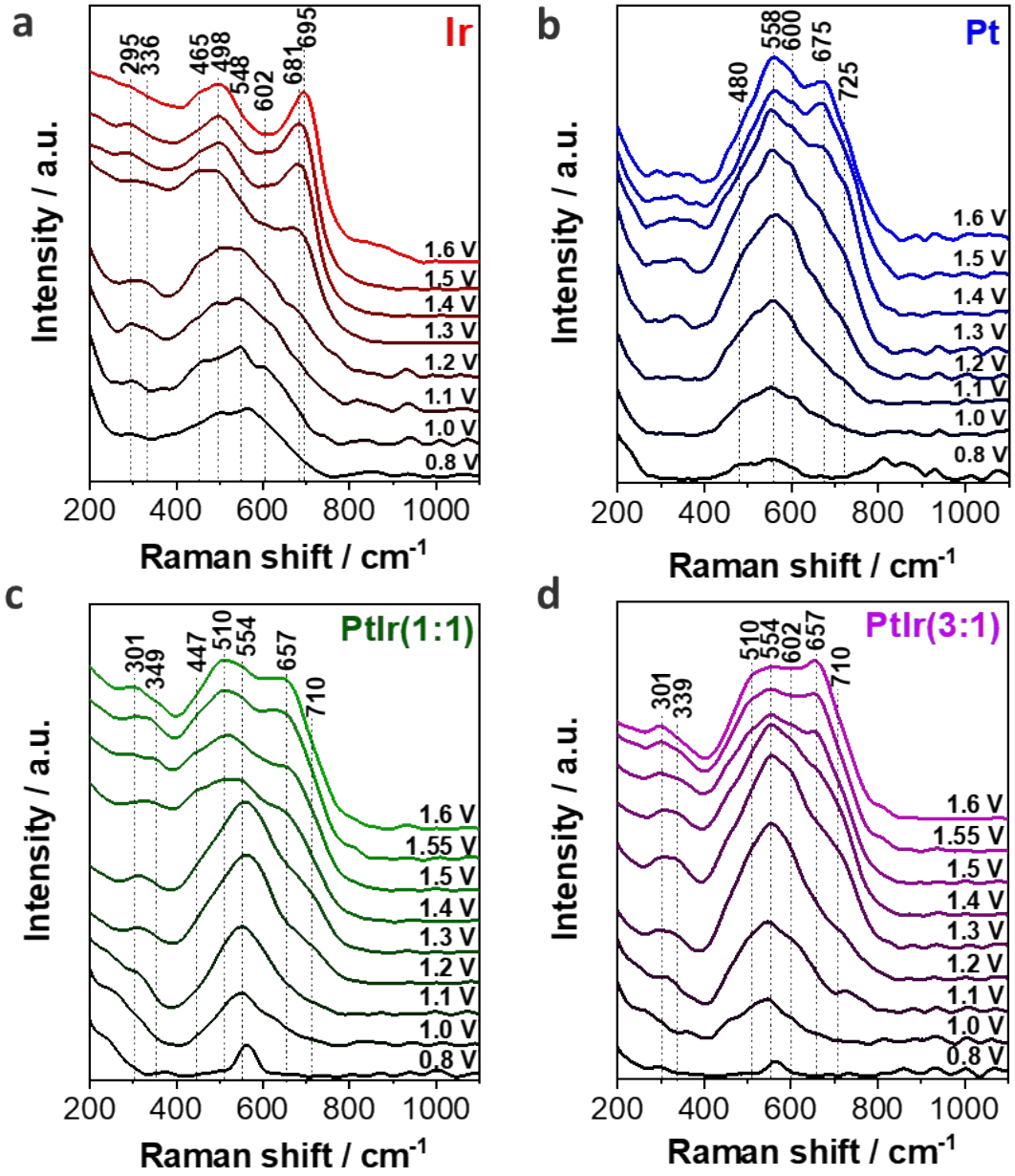

Fig. S9. Detailed evolution of potential-dependent series of Raman spectra for (**a**) Ir, (**b**) Pt, (**c**) PtIr(1:1) and (**d**) PtIr(3:1) thin films between 0.8 V_{RHE} and 1.6 V_{RHE} in 0.1 M $HClO_4$. Each potential was held for around 4 minutes, while Raman spectra were collected every 5 s and subsequently averaged. In **Tables 1-4** of the main manuscript, the peak assignments are listed.

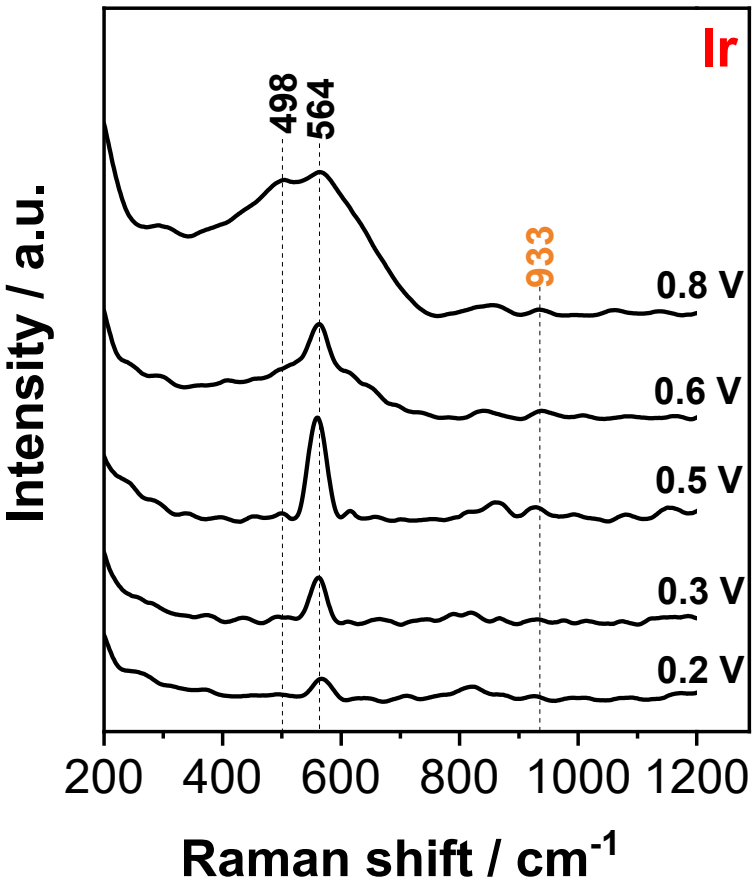

Fig. S10. In-situ Raman spectra collected from the monometallic Ir thin film in the potential range from 0.2 V_{RHE} to 0.8 V_{RHE} in 0.1 M $HClO_4$. The Raman band at 564 cm^{-1} is assigned to pure Ir^{3+}-OH and the evolution of the band at 498 cm^{-1} is associated with Ir^{4+} center formation.[4,13] The position at 933 cm^{-1} is labelled, where the adsorbed ClO_4^- anion is expected. Due to the low intensity and high background, it is likely in the noise level of the Raman signal.

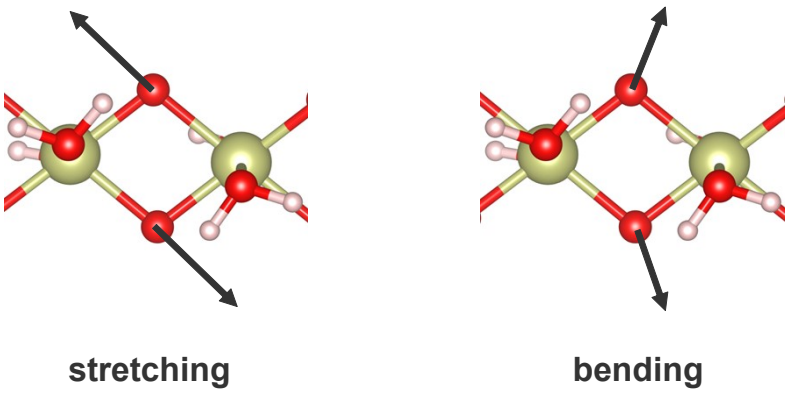

Fig. S11. Vibrations of the strong movement of the μ-oxo bonds. The arrows show the direction of the atomic movement of the stretching (left) and bending (right) motions. Iridium, oxygen and hydrogen are denoted with gold, red and white spheres, respectively.

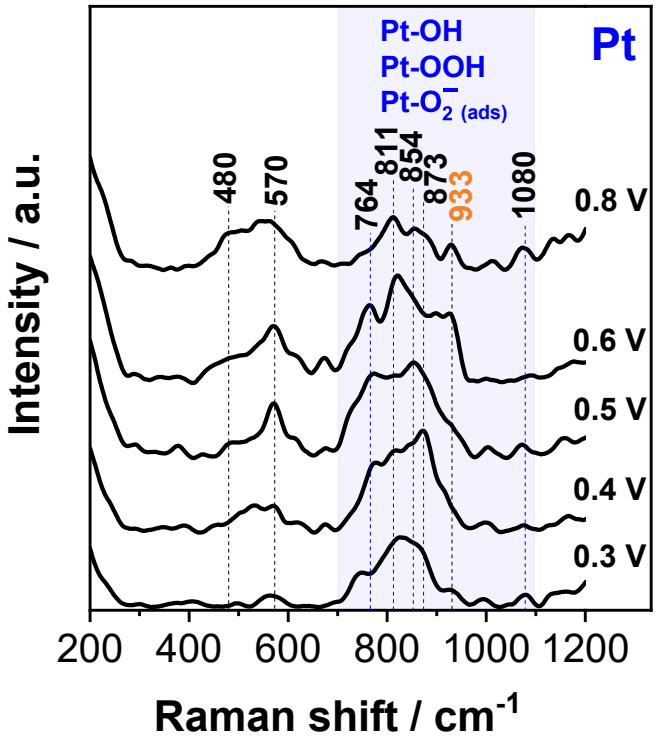

Fig. S12. Series of in-situ Raman spectra for the monometallic Pt thin film between 0.3 V_{RHE} and 0.8 V_{RHE} in 0.1 M $HClO_4$. The blue marked area shows the Raman shift region, where adsorbed oxygen species are expected.[9–12] Peak assignments are shown in **Table S6**.

Table S6. Summary of the Raman peaks for the monometallic Pt thin film between 0.3 V_{RHE} and 0.8 V_{RHE} (**Fig. S12**), corresponding modes of vibration and respective references of the assignments.

Raman shift / cm^{-1}	**Mode of vibration**	**Ref.**
480	Pt-O (oxide)	14
570	Pt-O (oxide)	9,12,15
764	$Pt\text{-}OOH_{(ads)}$	9–11
811	$Pt\text{-}O_{2\ (ads)}^{-}$	11,12
854	$Pt\text{-}O_{2\ (ads)}^{-}$	11,12
873	$Pt\text{-}O_{2\ (ads)}^{-}$	11,12
933	ClO_4^-	9–12
1080	$Pt\text{-}OH_{(ads)}$	10

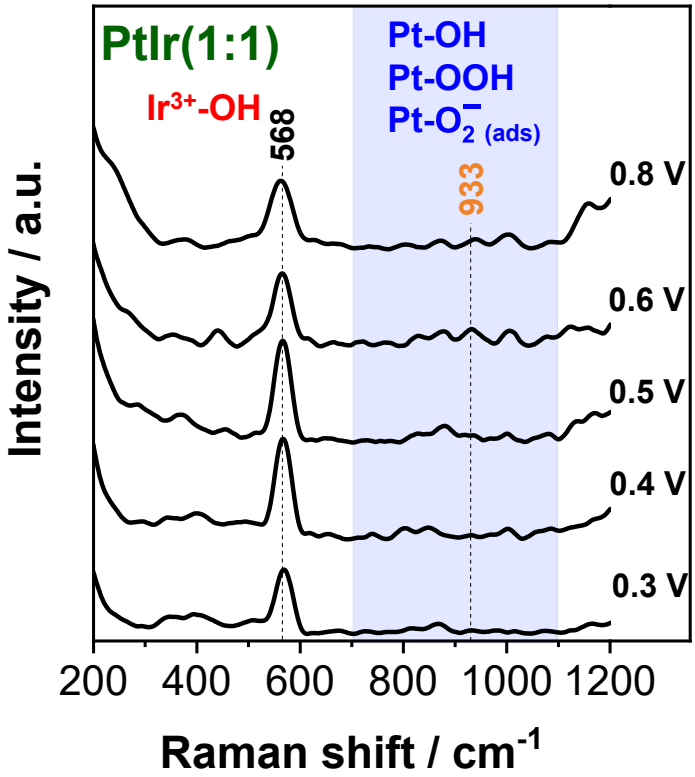

Fig. S13. In-situ Raman spectra collected from the PtIr(1:1) thin film by holding the potential from 0.3 V_{RHE} to 0.8 V_{RHE} with 100 mV steps in 0.1 M $HClO_4$. The Raman band at 568 cm^{-1} is assigned to Ir^{3+}-OH species (red). The expected formation of adsorbed oxygen species on platinum are denoted with a blue marked area.[9–12] At the Raman shift of 933 cm^{-1}, the adsorbed ClO_4^- anion might be expected, which is hidden in the signal-to-noise ratio.

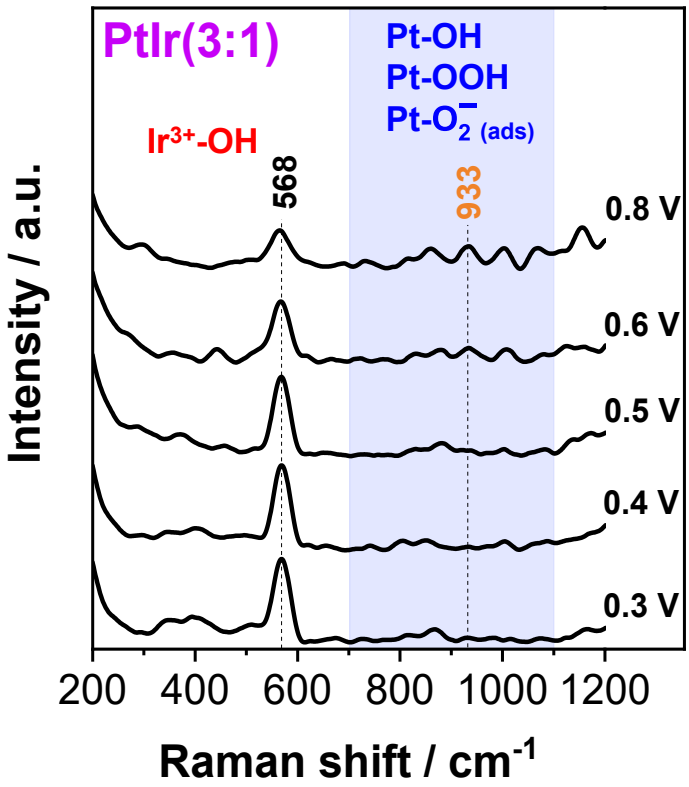

Fig. S14. Potential-resolved series of in-situ Raman spectra for the PtIr(3:1) thin film in 0.1 M $HClO_4$. The Ir^{3+}-OH species (red) is visible by the Raman band at 568 cm^{-1}. Due to the low intensity and high background, the peak at 933 cm^{-1} (orange label) assigned to adsorbed ClO_4^- anion is likely in the noise of the Raman data. The blue marked area shows the Raman shift region, where adsorbed oxygen species appear on the platinum surface.[9–12]

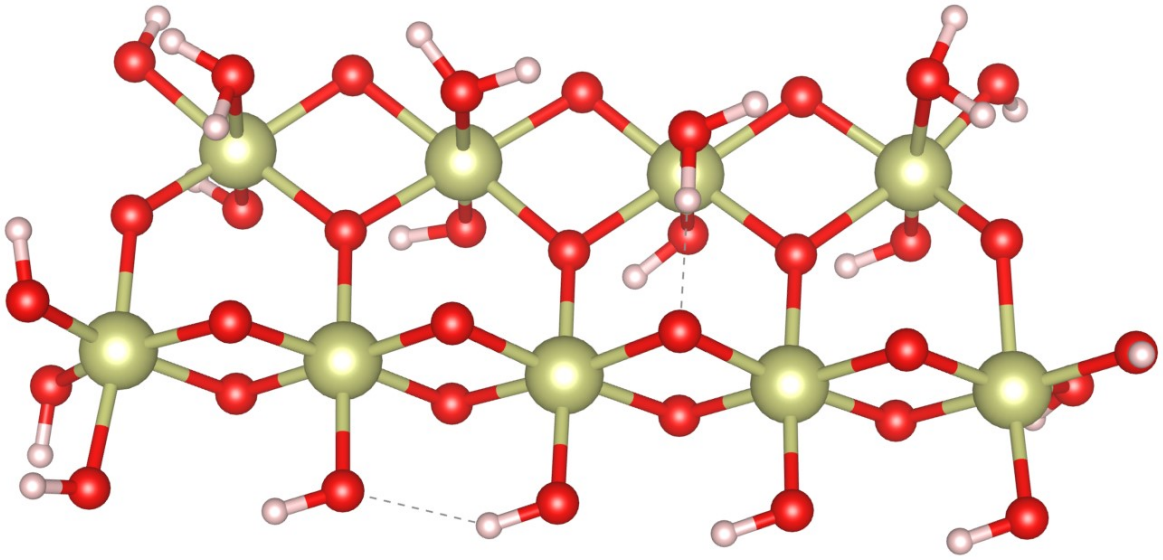

Fig. S15. Optimized 2D octamer geometry of the iridium oxo-hydroxo complex (67 atoms) used for the calculations of the predicted Raman spectrum in **Fig. S16**. Iridium, oxygen and hydrogen are denoted with gold, red and white spheres, respectively. For geometry optimization, the bottom -OH groups were fixed, allowing only the μ-oxo bridges and top-side H_2O molecules to freely vibrate.

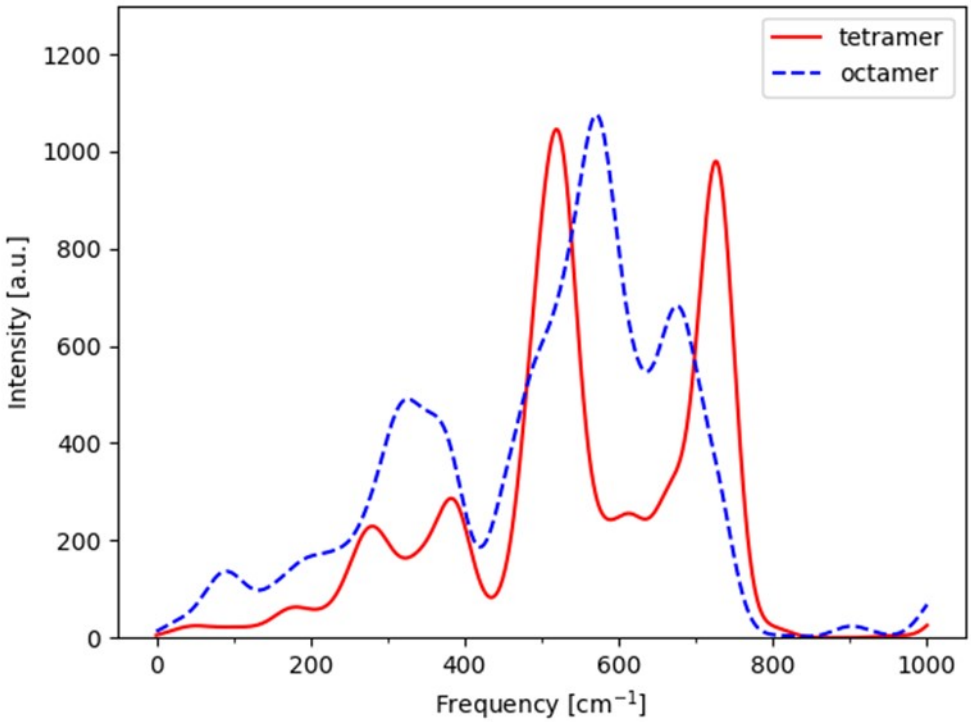

Fig. S16. Comparison of the DFT-based calculated Raman spectra of the iridium oxo-hydroxo complexes in a tetramer model with 38 atoms (red solid line) and 2D octamer model with 67 atoms (blue dashed line).

Table S7. Strongest DFT predicted Raman frequencies and modes of vibration for the iridium oxo-hydroxo complex shown in **Fig. 5a** of the main manuscript.

Raman shift / cm^{-1}	**Mode of vibration**
525	Ir-O-Ir antisymmetric stretch
725	Ir-O-Ir symmetric stretch

Table S8. According to the DFT calculations, strongest Raman frequencies and modes of vibration for the platinum oxo-hydroxo complex displayed in **Fig. 5b** of the main manuscript.

Raman shift / cm^{-1}	**Mode of vibration**
505	Pt-O-Pt antisymmetric stretch Pt-O-Pt bending
572	Pt-O-Pt symmetric stretch Pt-O-Pt bending
606	Pt-O-Pt symmetric stretch Pt-O-Pt bending
645	Pt-O-Pt symmetric stretch Pt-O-Pt bending

Table S9. Strongest DFT predicted Raman frequencies and modes of vibration for the platinum-iridium oxo-hydroxo complex with 1:1 Pt:Ir ratio, in **Fig. 5c**.

Raman shift / cm^{-1}	**Mode of vibration**
430	Ir-O-Pt bending
494	Ir-O-Pt bending
542	Ir-O-Pt bending Ir-O-Pt antisymmetric stretch
595/604	Ir-O-Pt bending
629	Ir-O-Pt bending Ir-O-Pt symmetric stretch
664	Ir-O-Pt symmetric stretch
682	Ir-O-Pt symmetric stretch

Table S10. Summary of the strongest DFT predicted Raman frequencies and the respective modes of vibration for the platinum-iridium oxo-hydroxo complex with 3:1 Pt:Ir ratio from **Fig. 5d.**

Raman shift / cm^{-1}	Mode of vibration
430	Ir-O-Pt bending
470	Ir-O-Pt bending
507	Ir-O-Pt symmetric stretch Ir-O-Pt bending Pt-O-Pt antisymmetric stretch
521	Pt-O-Pt bending Ir-O-Pt antisymmetric stretch Ir-O-Pt symmetric stretch
592/606	Ir-O-Pt symmetric stretch Pt-O-Pt symmetric stretch Pt-O-Pt symmetric stretch
620	Pt-O-Pt bending Ir-O-Pt bending

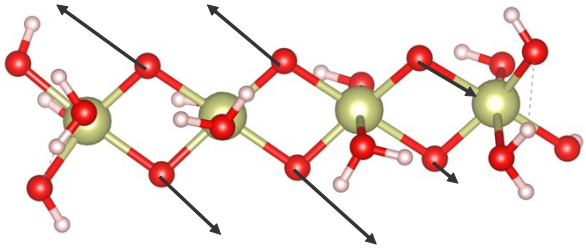

525 cm^{-1}

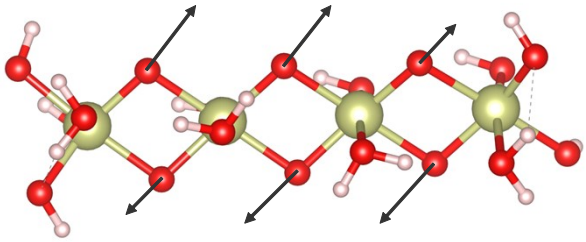

725 cm^{-1}

Fig. S17. Main DFT predicted modes of vibration of the strong movement for the μ-oxo bonds of the monometallic iridium oxo-hydroxo complex and the corresponding Raman shift. The arrows show the direction and magnitude of the atomic movement.

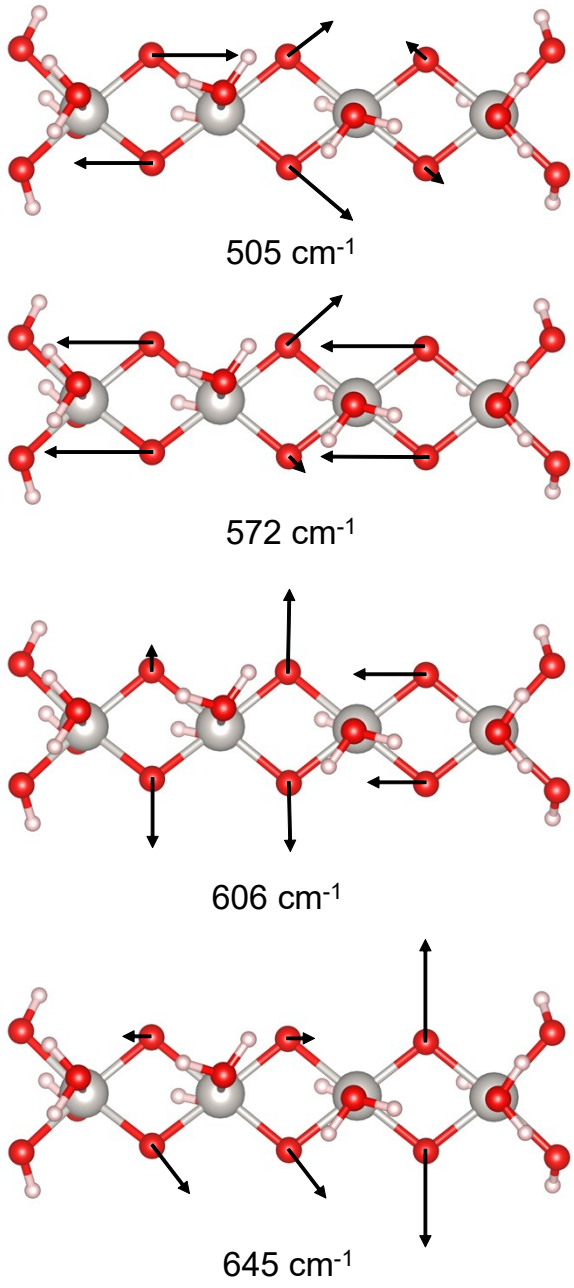

Fig. S18. Visualization of the vibrational modes of the strong movement of the μ-oxo bonds for the monometallic platinum oxo-hydroxo complex and the corresponding Raman shift based on the DFT calculations. The direction and magnitude of the atomic movement is denoted by black arrows.

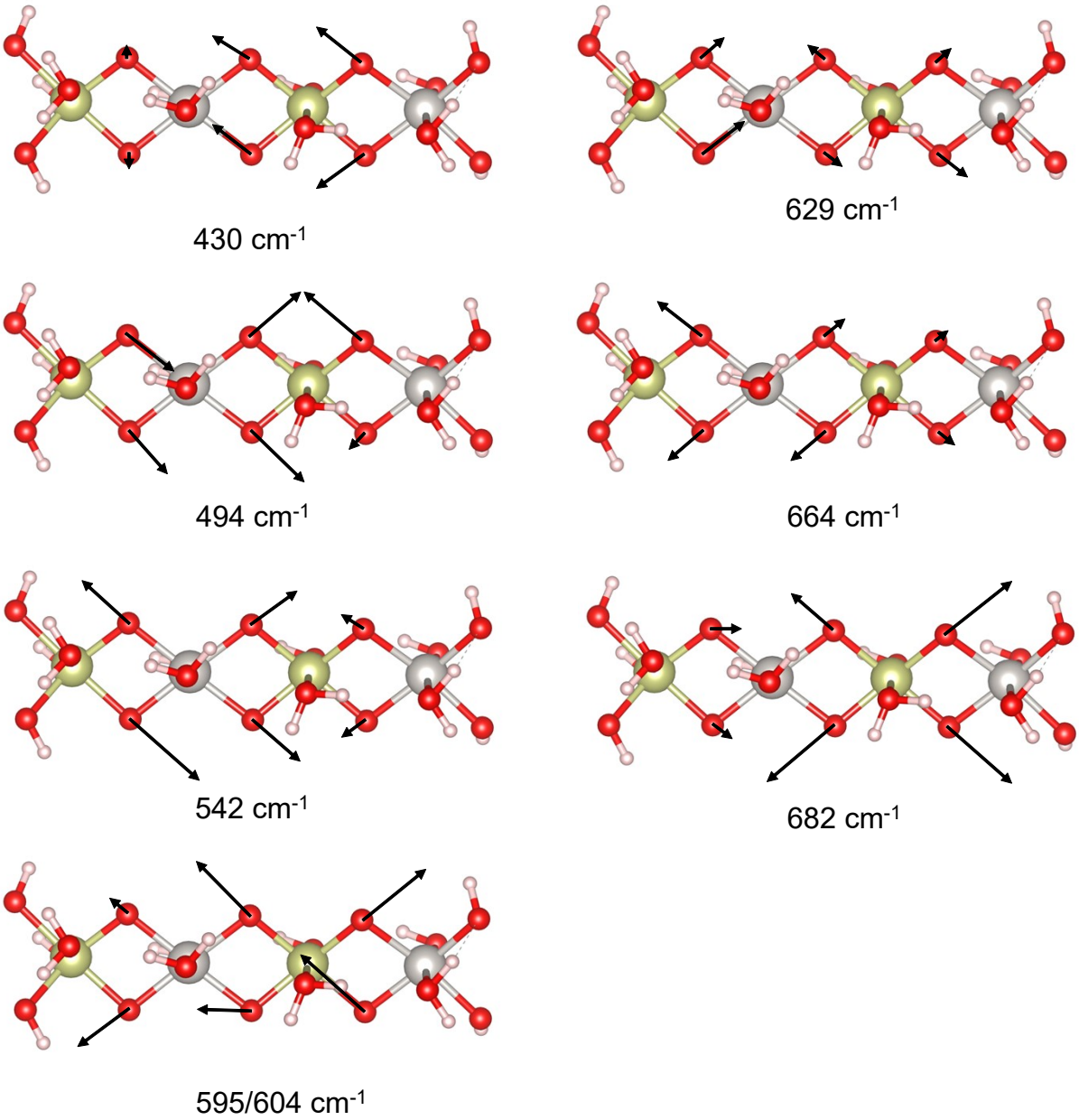

Fig. S19. Main DFT predicted modes of vibration of the strong movement of the μ-oxo bonds of the platinum-iridium oxo-hydroxo complex with Pt:Ir ratio of 1:1 and the corresponding Raman shift. The arrows show the direction and magnitude of the atomic movement.

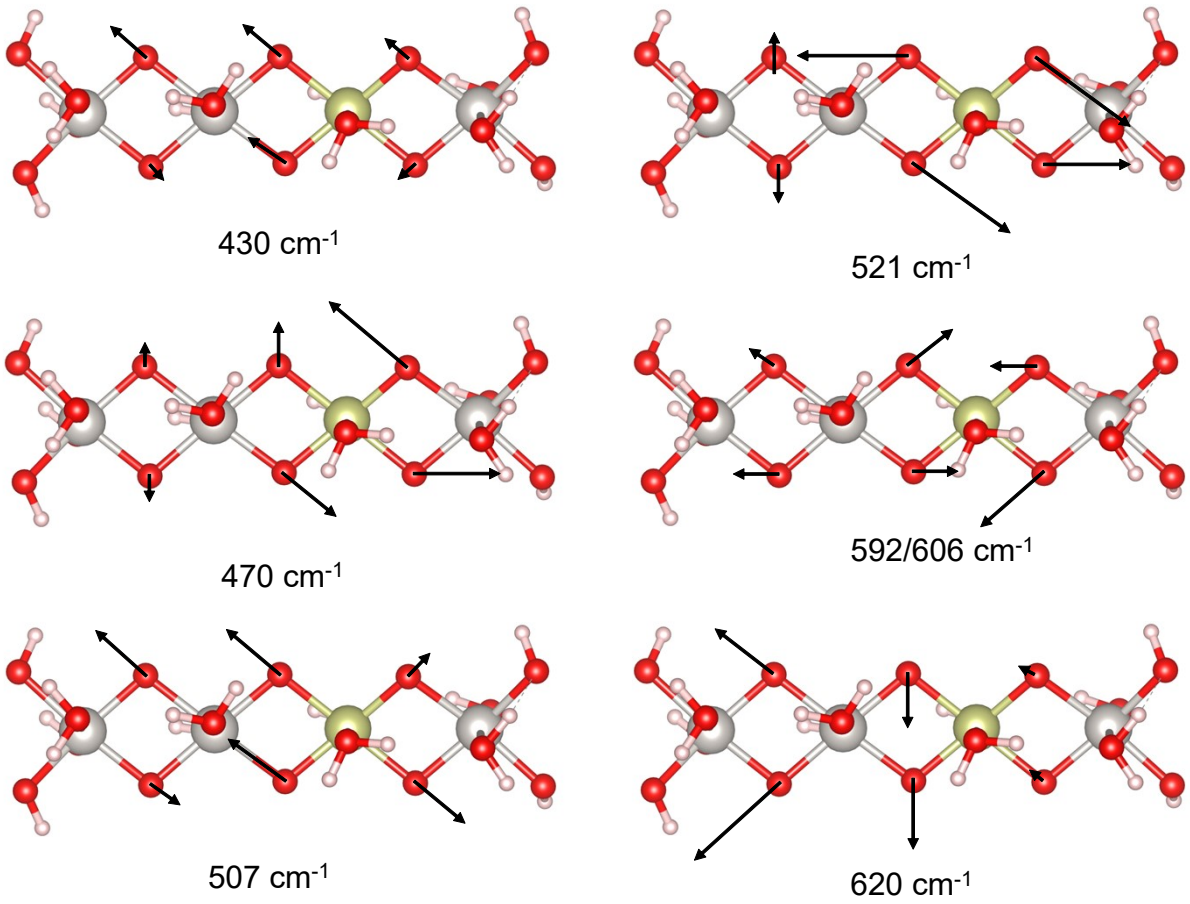

Fig. S20. The vibrational modes of the intensive movement of the μ-oxo bonds of the platinum-iridium oxo-hydroxo complex for the Pt:Ir ratio of 3:1. The arrows show the direction and magnitude of the atomic movement. The respective Raman shift is given below.

Table S11. Detailed comparison of the DFT predicted and experimental Raman shifts at for Ir,

Mode of vibration	DFT predicted Raman shift / cm^{-1}	Experimental Raman shift at 1.6 V_{RHE} / cm^{-1}
~~Mode of vibration~~	~~DFT predicted~~	~~Experimental Raman shift~~
Bimetallic PtIr(3:1)	**Raman shift / cm^{-1}**	**at 1.6 V_{RHE} / cm^{-1}**
~~Ir-O-Pt bending~~	~~430~~	~~-~~
Monometallic Ir		
~~Ir-O-Pt bending~~	~~470~~	~~-~~
Ir-O-Ir antisymmetric stretch Ir-O-Pt symmetric stretch	525	498
Ir-O-Ir symmetric stretch	725	695
~~Ir-O-Pt bending~~	~~507~~	~~510~~
Monometallic Pt		
Pt-O-Pt antisymmetric stretch Pt-O-Pt bending	505	Not observed in the broad band
Pt-O-Pt symmetric stretch Pt-O-Pt bending	572	600
Pt-O-Pt symmetric stretch Pt-O-Pt bending	606	600
Pt-O-Pt symmetric stretch Pt-O-Pt bending	645	675
Bimetallic PtIr(1:1)		
Ir-O-Pt bending	430	447
Ir-O-Pt bending	494	510
Ir-O-Pt bending Ir-O-Pt antisymmetric stretch	542	510 & 554
Ir-O-Pt bending	595/604	Plateau between 554 and 657
Ir-O-Pt bending Ir-O-Pt symmetric stretch	629	Plateau between 554 and 657
Ir-O-Pt symmetric stretch	664	657
Ir-O-Pt symmetric stretch	682	657

Pt, PtIr(1:1) and PtIr(3:1) at each vibrational mode by applying a potential of 1.6 V_{RHE}. Some experimental Raman bands appear very broad and not well resolved as individual vibrations.

Pt-O-Pt antisymmetric stretch		
Pt-O-Pt bending Ir-O-Pt antisymmetric stretch Ir-O-Pt symmetric stretch	521	550
Ir-O-Pt symmetric stretch Pt-O-Pt symmetric stretch Pt-O-Pt symmetric stretch	592/606	602
Pt-O-Pt bending Ir-O-Pt bending	620	657

Table S11. continued

References

(1) Merkys, A.; Vaitkus, A.; Grybauskas, A.; Konovalovas, A.; Quirós, M.; Gražulis, S. Graph isomorphism-based algorithm for cross-checking chemical and crystallographic descriptions. *Journal of cheminformatics* **2023**, *15* (1), 25. DOI: 10.1186/s13321-023-00692-1.

(2) Vaitkus, A.; Merkys, A.; Gražulis, S. Validation of the Crystallography Open Database using the Crystallographic Information Framework. *Journal of applied crystallography* **2021**, *54* (Pt 2), 661–672. DOI: 10.1107/S1600576720016532.

(3) Vaitkus, A.; Merkys, A.; Sander, T.; Quirós, M.; Thiessen, P. A.; Bolton, E. E.; Gražulis, S. A workflow for deriving chemical entities from crystallographic data and its application to the Crystallography Open Database. *Journal of cheminformatics* **2023**, *15* (1), 123. DOI: 10.1186/s13321-023-00780-2.

(4) Pavlovic, Z.; Ranjan, C.; Gao, Q.; van Gastel, M.; Schlögl, R. Probing the Structure of a Water-Oxidizing Anodic Iridium Oxide Catalyst using Raman Spectroscopy. *ACS Catal.* **2016**, *6* (12), 8098–8105. DOI: 10.1021/acscatal.6b02343.

(5) Moriau, L.; Nazrulla, M. A.; Logar, A.; Pavko, L.; Bele, M.; Hodnik, N.; Surca, A. K. Ir metal nanoparticles and IrO2 for acidic oxygen evolution reaction: Insight from Raman spectroscopy. *Sustainable Materials and Technologies* **2024**, *40*, e00901. DOI: 10.1016/j.susmat.2024.e00901.

(6) Zapata, F.; García-Ruiz, C. The discrimination of 72 nitrate, chlorate and perchlorate salts using IR and Raman spectroscopy. *Spectrochimica acta. Part A, Molecular and biomolecular spectroscopy* **2018**, *189*, 535–542. DOI: 10.1016/j.saa.2017.08.058. Published Online: Aug. 31, 2017.

(7) Huang, Y. S.; Lin, S. S.; Huang, C. R.; Lee, M. C.; Dann, T. E.; Chien, F. Z. Raman spectrum of IrO2. *Solid State Communications* **1989**, *70* (5), 517–522. DOI: 10.1016/0038-1098(89)90942-3.

(8) Liao, P.; Chen, C.; Ho, W.; Huang, Y.; Tiong, K. Characterization of IrO2 thin films by Raman spectroscopy. *Thin Solid Films* **1997**, *301* (1-2), 7–11. DOI: 10.1016/S0040-6090(96)09545-4.

(9) Dong, J.-C.; Su, M.; Briega-Martos, V.; Li, L.; Le, J.-B.; Radjenovic, P.; Zhou, X.-S.; Feliu, J. M.; Tian, Z.-Q.; Li, J.-F. Direct In Situ Raman Spectroscopic Evidence of Oxygen Reduction Reaction Intermediates at High-Index Pt(hkl) Surfaces. *J. Am. Chem. Soc.* **2020**, *142* (2), 715–719. DOI: 10.1021/jacs.9b12803. Published Online: Mar. 1, 2020.

(10) Dong, J.-C.; Zhang, X.-G.; Briega-Martos, V.; Jin, X.; Yang, J.; Chen, S.; Yang, Z.-L.; Wu, D.-Y.; Feliu, J. M.; Williams, C. T.; Tian, Z.-Q.; Li, J.-F. In situ Raman spectroscopic evidence for oxygen reduction reaction intermediates at platinum single-crystal surfaces. *Nat Energy* **2019**, *4* (1), 60–67. DOI: 10.1038/s41560-018-0292-z.

(11) Wang, Y.-H.; Le, J.-B.; Li, W.-Q.; Wei, J.; Radjenovic, P. M.; Zhang, H.; Zhou, X.-S.; Cheng, J.; Tian, Z.-Q.; Li, J.-F. In situ Spectroscopic Insight into the Origin of the Enhanced Performance of Bimetallic Nanocatalysts towards the Oxygen Reduction Reaction (ORR). *Angewandte Chemie International Edition* **2019**, *58* (45), 16062–16066. DOI: 10.1002/anie.201908907.

(12) Huang, Y.-F.; Kooyman, P. J.; Koper, M. T. M. Intermediate stages of electrochemical oxidation of single-crystalline platinum revealed by in situ Raman spectroscopy. *Nat Commun* **2016**, *7* (1), 12440. DOI: 10.1038/ncomms12440.

(13) Pavlovic, Z.; Ranjan, C.; van Gastel, M.; Schlögl, R. The active site for the water oxidising anodic iridium oxide probed through in situ Raman spectroscopy. *Chem. Commun.* **2017**, *53* (92), 12414–12417. DOI: 10.1039/C7CC05669A.
(14) Graham, G. W.; Weber, W. H.; McBride, J. R.; Peters, C. R. Raman investigation of simple and complex oxides of platinum. *J. Raman Spectrosc.* **1991**, *22* (1), 1–9. DOI: 10.1002/jrs.1250220102.
(15) Chan, H. Y. H.; Zou, S.; Weaver, M. J. Mechanistic Differences between Electrochemical and Gas-Phase Thermal Oxidation of Platinum-Group Transition Metals As Discerned by Surface-Enhanced Raman Spectroscopy. *J. Phys. Chem. B* **1999**, *103* (50), 11141–11151. DOI: 10.1021/jp992500o.